



Article

Improving the Pulse-Limited Footprint Resolution of GNSS-R Based on the Novel Joint Bandwidth Method

Zhen Cui ^{1,2,3,†} , Wei Zheng ^{1,4,5,6,7,*}, Fan Wu ^{3,†}, Xiaoping Li ¹, Keke Xu ⁵, Xiaofei Ma ², Jinwen Shi ², Xiao Tao ², Cheng Zhu ⁸ and Xingang Zhang ²

- ¹ School of Aerospace Science and Technology, Xidian University, Xi'an 710126, China; cuizhen@stu.xidian.edu.cn (Z.C.); xppli@xidian.edu.cn (X.L.)
 - ² Xian Institute of Space Radio Technology, China Academy of Space Technology, Xi'an 710100, China; maxf@cast504.com (X.M.); shijw@cast504.com (J.S.); taox@cast504.com (X.T.); zhangxg@cast504.com (X.Z.)
 - ³ Qian Xuesen Laboratory of Space Technology, China Academy of Space Technology, Beijing 100094, China; cuit@cast504.com
 - ⁴ China Academy of Aerospace Science and Innovation, Beijing 100176, China
 - ⁵ College of Surveying and Mapping and Land Information Engineering, Henan Polytechnic University, Jiaozuo 454003, China; xkk@hpu.edu.cn
 - ⁶ College of Electronic Information Engineering, Taiyuan University of Science and Technology, Taiyuan 030024, China
 - ⁷ School of Geomatics, Liaoning Technical University, Fuxin 123000, China
 - ⁸ School of Electronic Engineering, Xidian University, Xi'an 710071, China; zhcheng@mail.xidian.edu.cn
- * Correspondence: wzheng@xidian.edu.cn; Tel.: +86-159-10955262
† These authors contributed equally to this work.

Abstract: The bistatic global navigation satellite system's (GNSS) signal reflection technology has become an effective means of space-based sea surface wind field retrieval and height retrieval. By adopting a wider signal bandwidth, a higher pulse-limited footprint resolution can be achieved. However, for the GNSS-Reflectometry (GNSS-R) system, its signal bandwidth is affected by the signal bandwidth of the GNSS satellite, which limits the further improvement of the pulse-limited footprint resolution. This article proposes a method based on the novel signal bandwidth joint principle to improve the resolution of GNSS-R pulse-limited footprints. Firstly, currently in-orbit GNSS-R satellites use the traditional single frequency band (TSFB) method, which is limited by the GNSS satellite's signals and has a theoretical upper limit on its signal bandwidth. In response to this issue, this article proposes the novel joint bandwidth (NJBW) method (Galileo E5a and E5b signals) based on the auto-correlation function (ACF) signal ambiguity theory. The NJBW method reduces the main lobe width of the ACF of the GNSS-R signal by jointly processing the signals of E5a and E5b frequency bands, thus improving the pulse-limit footprint resolution of GNSS-R. Secondly, in order to verify the improvement effect of the novel joint bandwidth method on the pulse-limited footprint resolution of GNSS-R, this paper designs and fabricates an NJBW antenna verification prototype for the joint Galileo E5a and E5b frequency band and tests it in a microwave anechoic chamber. The test results indicate that the radio frequency (RF) bandwidth of the NJBW antenna validation prototype can cover both the frequency bands of E5a and E5b, making it suitable for use as the NJBW method for the GNSS-R receiving antenna. The bandwidth test values of the NJBW antenna validation prototype are consistent with the design values, which verifies the correctness of the NJBW antenna design model and further proves the feasibility of the NJBW method. Thirdly, based on the joint Galileo E5a and E5b frequency band signals, the NJBW method was applied to analyze the improvement effect of the pulse-limited footprint resolution. Compared to the TSFB method, the application of the NJBW method can increase the resolution of the GNSS-R pulse-limiting footprint by 1.73 times, which effectively improves the performance of the GNSS-R system. The NJBW method proposed in this article provides the theoretical method foundation and key technical support for sea surface wind field retrieval and height retrieval and the antenna design for the future high-precision and high pulse-limited footprint resolution GNSS-R sea surface wind field retrieval and height retrieval verification satellite.



Citation: Cui, Z.; Zheng, W.; Wu, F.; Li, X.; Xu, K.; Ma, X.; Shi, J.; Tao, X.; Zhu, C.; Zhang, X. Improving the Pulse-Limited Footprint Resolution of GNSS-R Based on the Novel Joint Bandwidth Method. *Remote Sens.* **2023**, *15*, 4118. <https://doi.org/10.3390/rs15174118>

Academic Editor: Chung-yen Kuo

Received: 18 July 2023

Revised: 18 August 2023

Accepted: 19 August 2023

Published: 22 August 2023



Copyright: © 2023 by the authors. Licensee MDPI, Basel, Switzerland. This article is an open access article distributed under the terms and conditions of the Creative Commons Attribution (CC BY) license (<https://creativecommons.org/licenses/by/4.0/>).

Keywords: novel joint bandwidth method; pulse-limited footprint resolution; GNSS-R sea surface wind field retrieval and height retrieval; antenna validation prototype; Galileo/GNSS-R satellite

1. Introduction

In recent years, GNSS signals have been found to be applicable to various environmental remote sensing technologies. For example, Martin-Neira (1993), Katzberg et al. (1996), and Garrison et al. (1997, 1998) found that the multipath effect of GNSS signals reflected from the sea surface can serve as a new tool for ocean remote sensing [1–4]. A GNSS reflection signal receiver is arranged in the Earth’s orbit to form the GNSS-R system, and a series of remote sensing applications can be carried out by using the GNSS reflection signals. Among these remote sensing applications, sea surface wind field retrieval and height retrieval has become a popular field of GNSS-R remote sensing in recent years.

The traditional sea surface remote sensing method adopts the monostatic radar method, which requires specialized transmitters, receivers, and large directional antennas to achieve high resolution [5–8]. The GNSS-R studied in this article is a bistatic radar system that only requires a receiver and does not need a transmitter, as GNSS satellites provide transmission signals. The bistatic structure of the GNSS-R system and the uniqueness of the GNSS signal determine that the GNSS-R system can obtain relevant feature parameters of the sea surface in the mesoscale range without using large directional antennas. This characteristic is one of the advantages of the GNSS-R sea surface wind field retrieval system and sea surface height retrieval system.

Martin-Neira (1993) was the first to propose and describe a bistatic GNSS-R system using GPS signals [1]. Subsequently, Auber et al. (1994) unexpectedly obtained GPS reflection signals on airborne platforms and reported them [9]. These potential remote sensing signals of the ionosphere and sea surface were discovered by Katzberg et al. (1996) [2]. They first theoretically predicted the changes in GPS signals reflected by the sea surface and land, and then Garrison et al. (1997, 1998) demonstrated the feasibility of using left-handed circularly polarized (LHCP) antennas and traditional GPS receivers to track GNSS reflected signals in airborne experiments [3,4]. In addition, National Aeronautics and Space Administration (NASA) also proposed using a low-altitude orbit receiving platform to collect GPS signals reflected by the sea surface and used delay mapping receivers to carry out airborne flight tests under different sea surface conditions many times [10–12]. The relationship between the reflected signal power curve and the sea surface roughness under different time delays was analyzed, and the theoretical and experimental basis for using the GPS-reflected signal under airborne conditions to retrieve the sea surface wind speed was preliminarily established. Elfouhaily et al. (1997) established a unified directional spectrum of long-wave and short-wave driven by wind on the basis of previous research [13], which laid a certain foundation for the theoretical model research of sea surface wind field retrieval. Zavorotny et al. (2000) proposed a mature and widely used time-delay and Doppler two-dimensional power model of GPS-reflected signals through the systematic analysis of sea wind detection of GPS-reflected signals, using the bistatic radar equation combined with the geometrical optics approximation principle, which is the Z-V model [14], providing a theoretical basis for GNSS-R-based sea wind detection. Zuffda et al. (2003) used theoretical models and actual airborne data to analyze the sensitivity of GPS reflection signal-related power curves to sea surface wind speed and direction, receiver platform height, satellite elevation angle, and receiver coherent integration time, providing a specific and clear theoretical basis for better sea surface wind field retrieval experiments [15]. The University of Colorado, NASA, the European Space Agency (ESA), and Spain’s Starlab have also carried out a large number of experiments, including experiments on receiving platforms such as airborne, spaceborne, and hot air balloons. The waveform is matched with the waveform obtained from the actual test to obtain the wind field information, and the results are compared and analyzed. In recent years, in addition to waveform matching, delay-

Doppler map (DDM) deconvolution and DDM-related geometric parameter extraction methods have been proposed for wind field retrieval methods under airborne conditions. Valencia et al. (2011) used the method of image processing to deconvolute the DDM to obtain the scattering coefficient, estimated the mean square slope of the sea surface by using the scattering coefficient, and carried out wind field retrieval according to the relationship between the mean square slope and the wind speed and direction of the sea surface [16]. In terms of spaceborne platforms, Gleason et al. (2005) used the measured data to specifically analyze the change in signal-to-noise ratio (SNR) and the corresponding measurement accuracy under different spaceborne platforms' heights and antenna configurations [17]. Li et al. (2014) carried out the wind field retrieval under spaceborne conditions by using the two-dimensional least squares fitting method and the variable length iterative method to determine the parameters [18]. Clarizia et al. (2015) analyzed the average value, variance, front slope, tail slope, and other variables of the on-board DDM and obtained the empirical relationship with wind speed through regression fitting [19].

At present, the feasibility (that is, the sensitivity) of GNSS-R sea surface wind field retrieval and height retrieval technology has been verified, and further improvement of pulse-limited footprint resolution is the key to realizing GNSS-R applications. High pulse-limited footprint resolution GNSS-R sea surface wind field retrieval and height retrieval data can effectively improve the clarity of the ocean physical model it retrieves, which is of great significance for the fine-grained study of ocean motion [20]. The research team of navigation and detection based on the information of aerospace–aeronautics–marine integration of Qian Xuesen Laboratory of Space Technology (Qian Lab) has carried out the acquisition of a high-precision and high pulse-limited footprint resolution ocean gravity field based on spaceborne GNSS-R measurement methods and then prospective research on theoretical methods and key technologies for improving the underwater gravity matching navigation accuracy [21–30]. Wu et al. (2019) conducted research on improving the positioning accuracy of GNSS-R mirror reflection points using the combination correction method of a gravity field normal projection reflection reference plane [21]. Wu et al. (2019) conducted research on improving the positioning accuracy of a satellite-borne GNSS-R specular reflection point on the sea surface based on the ocean tidal time-varying elevation correction positioning method [22]. Liu et al. (2019) conducted research on improving the number of sea surface altimetry reflected signals received by the GNSS-R satellite based on the new satellite-borne nadir antenna receiving a signal-to-noise ratio model [23]. Wu et al. (2021) conducted research on improving the specular point positioning accuracy of ship-borne GNSS-R observations in China's seas based on a new instantaneous sea reflection surface model [24]. Cui et al. (2021) conducted research on improving GNSS-R sea surface altimetry precision based on the novel dual circularly polarized phased array antenna model [25]. Wang et al. (2021) proposed a new GNSS-R altimetry algorithm based on a machine learning fusion model and feature optimization to improve the precision of sea surface height retrieval [26]. Sun et al. (2021) conducted research on improving the iGNSS-R ocean altimetric precision based on the coherent integration time optimization model [27]. Liu et al. (2021) conducted research on the relationship between altimetric quality and along-track spatial resolution for iGNSS-R sea surface altimetry based on the airborne experiment [28]. Yan et al. (2022) proposed a correction method of atmospheric delay error of airborne and spaceborne GNSS-R sea surface altimetry [29]. Wang et al. (2022) conducted research on improving the SSH retrieval precision of spaceborne GNSS-R based on a new grid search multihidden layer neural network feature optimization method [30]. Obtaining high precision and high pulse-limited footprint resolution sea surface information based on spaceborne GNSS-R technology is one of the key technologies among them.

According to the different signal processing methods for obtaining remote sensing information, GNSS-R sea surface wind field retrieval and height retrieval is mainly divided into cGNSS-R (conventional GNSS-R) [31] and iGNSS-R [1]. The cGNSS-R obtains remote sensing information by correlating the reflected signal with a locally generated copy of the transmitted signal after Doppler frequency shift compensation for a certain period

of time (usually 1 ms). Currently realized spaceborne GNSS-R missions all use cGNSS-R technology, such as UK-DMC (UK Disaster Monitoring Constellation, launched on 27 September 2003 [32]), TDS-1 (TechDemoSat-1, launched on 8 July 2014 [33]), 3Cat-2 (launched on 15 August 2016 [34]), CYGNSS (Cyclone Global Navigation Satellite System, launched on 15 December 2016 [35]), and BuFeng-1 Constellation (launched on 5 June 2019 [36]). However, since the above spaceborne GNSS-R missions all use a single C/A code frequency band, its bandwidth (2.046 MHz) is relatively narrow, which limits its pulse-limited footprint resolution [37]. In order to overcome the bandwidth limitation, Martin-Neira et al. proposed the iGNSS-R concept and related models [1,38]. The iGNSS-R does not need to obtain the structure of the ranging code, and the iGNSS-R system directly correlates the reflected signal with the direct signal to obtain the remote sensing information. Therefore, iGNSS-R technology can extract all the spectral components in the GNSS-transmitted signal, improve the definition of the ACF, and thus improve the pulse-limited footprint resolution [39]. However, the performance of the iGNSS-R sea surface wind field retrieval and height retrieval is also directly related to the SNR. Due to the correlation between the direct signal and the reflected signal, and the increase in signal bandwidth bringing higher thermal noise, it is necessary to use the direct/reflected signal receiver antennas of higher gain to improve SNR. In addition, the iGNSS-R cannot distinguish GNSS satellites according to the code structure and requires the antenna to synthesize multiple beams with variable orientation to simultaneously capture and track multiple GNSS reflection signals. Therefore, the spaceborne iGNSS-R sea surface wind field retrieval or height retrieval task is more suitable to use a high-gain (directivity greater than 20 dBi) digital multi-beam phased array antenna, which makes the iGNSS-R system more complex than the cGNSS-R system, and the cost is also more expensive. In addition, due to the limitation of the GNSS signal bandwidth, even if the iGNSS-R method based on a single frequency band is carried out, the bandwidth is still in the range of 25 MHz, and the corresponding spatial resolution is ~ 4 km, which is in contrast to the mission of high pulse-limited footprint resolution sea surface wind field retrieval and height retrieval in the future. However, there is still a certain gap in the 2 km level pulse-limited footprint resolution requirements of the mission.

With the development of GNSS signals, in order to optimize tracking performance, GNSS systems have introduced new signal modulation methods and wider frequency band signals. Among them, the Galileo satellite navigation system uses the ALT-BOC signal modulation method, with the E5 frequency band signal as the background, and the E5a (lower) and E5b (upper) signal components on the two frequency sub-bands form a multi-carrier composite broadband (51.15 MHz) signal. The bandwidth of the E5 signal is more than double that of the previous GNSS signal, which provides a new opportunity for improving the pulse-limited footprint resolution of spaceborne GNSS-R sea surface wind field retrieval and height retrieval. In addition, the encoding method of Galileo E5a and E5b signals is open, which allows the GNSS-R system based on E5a and E5b signals to adopt the cGNSS-R method, thereby reducing the complexity and cost of GNSS-R systems while ensuring the performance of sea surface wind field retrieval and height retrieval.

Different from the previous studies, this article adopts the NJBW method based on the Galileo/GNSS-R signal to conduct research on the pulse-limited footprint resolution of GNSS-R sea surface wind field retrieval and height retrieval. First, based on the ambiguity function of the bistatic radar equation, the NJBW method is proposed. Second, in order to verify the correctness of the analysis results of the GNSS-R pulse-limited footprint resolution based on the NJBW method, this article fabricated a GNSS-R NJBW antenna verification prototype and tested it in a microwave anechoic chamber. The test results are consistent with the design values, which prove the correctness of the analysis results. Third, the test results of the GNSS-R NJBW antenna verification prototype were brought into the spaceborne sea surface wind field retrieval and height retrieval scenario, and the pulse-limited footprint resolution of the GNSS-R sea surface wind field retrieval and height retrieval was evaluated. The evaluation results show that the pulse-limited footprint

resolution can be increased by 1.73 times by using the Galileo/GNSS-R NJBW method to retrieve the sea surface wind field.

2. Methods

2.1. Size of Pulse-Limited Footprint

In this article, we use the theoretical model proposed by Zavorotny et al. (2000) [14] to predict the structure of the reflected signal received by the GNSS-R receiver after the GNSS signal is reflected by the sea surface. The schematic diagram of the GNSS-R system is shown in Figure 1. In the GNSS-R scene shown in Figure 1, the strongest scattering signal only comes from a limited area around a nominally specular reflection point at sea surface (that is, the “glistening zone”). The scattering signal outside the glistening zone is very weakly Bragg scattering, so this article does not consider this scattering term. The above physical background makes us use the geometrical optics limit of the Kirchhoff approximation to carry out the theoretical modeling of GNSS scattering signals.

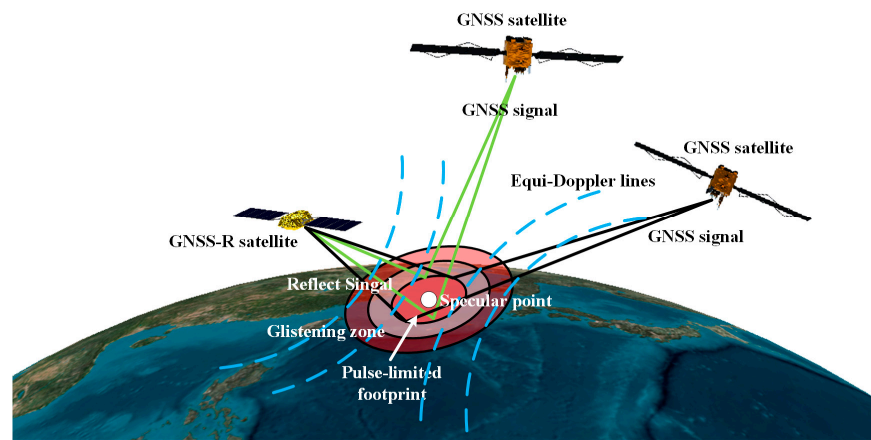


Figure 1. GNSS-R system schematic diagram.

This article adopts a GNSS-R signal model based on Kirchhoff approximation, which was adopted by Beckham et al. (1987), Rytov et al. (1988), Clifford et al. (1998), Bass et al. (2013), and Voronovich et al. (2013) and is suitable for short-wavelength, bistatic, and rough surface scattering problems [40–44]. Kirchhoff approximation indicates that a relatively “smooth” small piece of rough surface sample can be approximated as the tangent plane of any point on the sample. For a certain moment t_0 , the cross-correlation coefficient of the received reflected signal u to different delay τ can be expressed as integral [14]

$$Y(t_0, \tau) = \int_0^{T_i} a(t_0 + t')u(t_0 + t' + \tau)e^{2\pi if_c t'} dt' \quad (1)$$

where T_i represents the integration time, and $a(t)$ represents the waveform of the direct GNSS signal within the time period τ_c of one chip. In addition, f_c represents the frequency offset factor, which is used to compensate the Doppler frequency offset of the reflected signal. It can be known from Equation (1) that the maximum cross-correlation value of the direct signal waveform $a(t)$ and the reflected signal waveform $u(t)$ occurs at the Doppler frequency offset, and this frequency offset has been fully compensated, and the time series of the two signals are completely aligned.

A coordinate system was established as shown in Figure 2, where the specular point is the origin of the coordinate system, the XOY plane is the tangent plane of the Earth’s surface passing through the specular point, and the z-axis is the normal direction of the specular point. The scattered GNSS signal reaching the GNSS-R receiver can be modeled by integrating over the mean sea surface [45]:

$$u(t) = \int D(\vec{\rho}) \cdot a\left(t - \frac{R_T(t) + R_R(t)}{c}\right) \cdot g(\vec{\rho}, t) d^2\rho \quad (2)$$

where $D(\vec{\rho})$ represents the gain of the GNSS-R receiving antenna in the direction $\vec{\rho}$ of the scattering point, $a(t)$ represents the PRN code function, and c represents the speed of light. $R_T(t)$ and $R_R(t)$ represent the distance from any scatter point in the glistening zone to the transmitter and receiver, respectively, where the coordinates of the scatter point are $(\vec{\rho}, z)$, where $z = \zeta(\vec{\rho}, t)$ represents the altitude of the scatter point [14]. In the above discussion, since the size of the glistening zone is usually small, the sea surface in the glistening zone can be considered approximately as a plane. In addition, the sea surface in the glistening zone can be considered as a small piece of flat sea surface, as we are ignoring the Earth's arc of the glistening zone. Therefore, it can be considered that $\vec{\rho} = (x, y)$, where x and y represent the coordinates of the scatter point on the Earth's surface, respectively, and z represents the altitude of the scatter point.

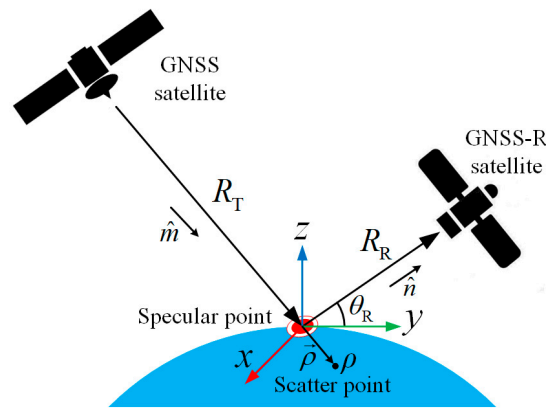


Figure 2. Geometric relationship of GNSS-R system.

In addition, the g in Equation (2) represents the propagation and scattering process [46]

$$g(\vec{\rho}, t) = -\frac{V(\vec{\rho}) \cdot q^2 \cdot e^{ik(R_T(t)+R_R(t))}}{4\pi i R_T(t) R_R(t) q_z} \tag{3}$$

where V represents the Fresnel reflection coefficient; $\vec{q} = k(\hat{n} - \hat{m})$ represents the scattering vector, where $k = 2\pi/\lambda$ represents the radiation wave number; and q_z represents the modulus of the normal component of the scattering vector \vec{q} at the specular point; \hat{m} represents the unit vector of the incident wave, \hat{n} represents the unit vector of the scattered wave; i represents an imaginary unit whose value is equal to $\sqrt{-1}$. Substituting Equation (3) into Equation (2) and then into Equation (1), the instantaneous signal can be expressed as Equation (4) [14]:

$$Y(t_0, \tau) = T_i \int D(\vec{\rho}) \Lambda\left(\tau - \frac{R_T + R_R}{c}\right) S(\Delta f(\vec{\rho})) g(\rho, t_0) d^2\rho \tag{4}$$

where function Λ represents the ACF of the PRN code transmitted by GNSS satellite [45]:

$$\Lambda(\tau) = \frac{1}{T_i} \int_0^{T_i} a(t) a(t + \tau) dt \tag{5}$$

The Doppler-spread function can be approximately expressed as a sinc function [45]:

$$|S(\Delta f)| = \text{sinc}(\Delta f T_i) = \frac{\sin(\pi \Delta f T_i)}{\pi \Delta f T_i} \tag{6}$$

The greatest cross-correlation value of the received reflected signal with the signal replica $a(t)$ within the GNSS-R satellite occurs when the Doppler shift compensated signal is aligned with the receiver's replica $a(t)$. If the received signal is reflected from the sea surface, the reflected signal $u(t)$ can be expressed as the sum of multiple paths, which

contain different time delays and different Doppler shifts. According to Equation (5) and Equation (6), only when the time delay and Doppler shift of the direct signal and the reflected signal are corrected can the maximum value of the cross-correlation function between them be obtained. The same time delay corresponds to the concentric rings in the glistening zone on the sea surface, and this zone can be calculated by obtaining the navigation and positioning signal through the GNSS direct signal link of the GNSS-R satellite. Finally, the average power of the delayed signal can be obtained by averaging its inner product over the integration time T_i [45]

$$\langle |Y(\tau)|^2 \rangle = \frac{1}{T_i} \int_0^{T_i} |Y(t_0, \tau)|^2 dt_0 \quad (7)$$

Substituting Equation (4) into Equation (7), the average power expression about time delay τ and frequency shift Δf can be obtained. Assuming that the altitude of each scattering point in the glistening zone is consistent within the cumulative time T_i , Equation (8) can be obtained [45]:

$$\langle |Y(\tau)|^2 \rangle = T_i^2 \iint \frac{D^2(\vec{\rho}) \Lambda^2 \left(\tau - \frac{R_T + R_R}{c} \right) \left| S(\Delta f(\vec{\rho})) \right|^2}{4\pi R_T^2 R_R^2} \sigma_{0,b}(\vec{q}(\vec{\rho})) d^2\rho \quad (8)$$

This equation is called the bistatic radar equation [39], where $\sigma_{0,b}(\vec{q}(\vec{\rho}))$ represents the normalized bistatic scattering cross-section of the sea surface at the scatter point $\vec{\rho}$, where $\vec{q}(\vec{\rho})$ represents the scatter vector at the scatter point $\vec{\rho}$. In addition, the

$$D^2(\vec{\rho}) \Lambda^2 \left(\tau - \frac{R_T + R_R}{c} \right) \left| S(\Delta f(\vec{\rho})) \right|^2 \quad (9)$$

in Equation (8) represents the pulse-limited footprint.

In the research of this paper, some simplifications can be made. Since a low-gain antenna is used in cGNSS-R satellite, it can be approximately considered that the gain of the antenna in the glistening zone $D(\vec{\rho})$ is constant (to simplify the analysis, we set $D(\vec{\rho}) = 1$). Therefore, the integral factor $D^2(\vec{\rho})$ which represents the antenna's gain in Equation (8) can be removed. If the frequency difference between the Doppler shift and the compensation frequency Δf remains 0 in the glistening zone, the variable $S(\Delta f(\vec{\rho}))$ according to Equation (6) is close to 1, which indicates complete Doppler shift compensation. In the typical case of altitude, velocity, and number of integrations for a GNSS receiver, the integration time T_i is ~ 1 ms. Therefore, it can be further assumed that $S(\Delta f(\vec{\rho})) = 1$. After the above rational simplification, the only factor that determines the size of the pulse-limited footprint in this paper is Λ^2 .

2.2. Galileo/GNSS-R NJBW Method

This article considers the width of the ACF of PRN signals. In general, the main power of the ACF Λ is concentrated in its main lobe, so when analyzing the size of the pulse-limited footprint, the main lobe width of Λ is mainly considered. According to the Wiener–Khinchin theorem, the ACF of a PRN signal is the Fourier transform of its power spectral density (PSD) [47]

$$\Lambda_{\text{PRN}}(\tau) = F\{P_{\text{PRN}}(f)\} \quad (10)$$

where $\Lambda_{\text{PRN}}(\tau)$ represents the ACF of the PRN signal, $F\{\cdot\}$ represents the Fourier transform operator, and $P_{\text{PRN}}(f)$ represents the PSD of the PRN signal. The PRN signal can be considered as a BPSK or QPSK signal, and its PSD can be considered as a sinc square function [48]

$$P_{\text{PRN}}(f) = \frac{1}{f_s} \left| \text{sinc} \left(\frac{f - f_c}{f_s} \right) \right|^2 \quad (11)$$

where f_s represents the signal bandwidth, and f_c represents the center frequency of the carrier. It is known that the Fourier transform of the sinc square function is a triangular wave function [49]

$$F \left\{ \left| \text{sinc} \left(\frac{f - f_c}{f_s} \right) \right|^2 \right\} = \text{tri}(\tau f_s) = \begin{cases} f_s \left(1 - \frac{|\tau|}{f_s} \right), & \tau < \frac{1}{f_s} \\ 0, & \text{else} \end{cases} \quad (12)$$

where $\text{tri}(\tau f_s)$ represents the triangular wave function model whose base length is $\frac{2}{f_s}$ (that is, from $-\frac{1}{f_s}$ to $\frac{1}{f_s}$). Therefore, its main lobe width is $\frac{2}{f_s}$.

Substituting Equation (12) and Equation (11) into Equation (10), the ACF expression of the PRN signal can be obtained as

$$\Lambda_{\text{PRN}}(\tau) = \frac{1}{f_s} \cdot \text{tri}(\tau f_s) \quad (13)$$

It can be known from Equation (13) that the main lobe width of the PRN signal ACF is inversely proportional to the signal bandwidth f_s . By increasing the signal bandwidth, the main lobe width of the PRN signal ACF can be reduced. However, in the GNSS-R system, the PRN signal transmits from the GNSS satellite, and its PRN signal bandwidth is affected by the GNSS satellite signal bandwidth. Thus, there is a theoretical upper limit to the main lobe width of the ACF when using the TSFB transmitted by GNSS satellite. However, fortunately, there are some signals with basically the same signal structure in GNSS satellites. Jointing multiple signals among them can form a NJBW joint signal, which has an equivalent wider bandwidth function than the TSFB GNSS signal.

The E5 band signal of Galileo navigation system is a group of signals with the above characteristics, as shown in Figure 3. It consists of two signal bands of the E5a and the E5b, which are broadcast at two center frequencies of 1176.45 MHz and 1207.14 MHz, respectively [50,51]. Both E5a and E5b consist of two-phase quadrature components, and the alternate binary offset carrier (ALT-BOC) technique is used to joint the E5a signal and the E5b signal into one constant envelope signal. The E5a signal is the lower sideband of ALT-BOC (E5a/b), which can be regarded as QPSK (10), where data and pilot are orthogonal; the E5b signal is the upper sideband of the E5 signal, and its orthogonal components E5bI and E5bQ can be seen as BPSK. The bandwidth of both E5a and E5b signals is 20.46 MHz. According to their signal frequency bands, when the two signals are jointed into a broadband signal (E5a/b NJBW joint signal), the bandwidth can be 51.15 MHz, which is the maximum bandwidth that GNSS signals are available at, at present. It is beneficial to improve the retrieval performance of GNSS-R sea surface wind field and height retrieval.

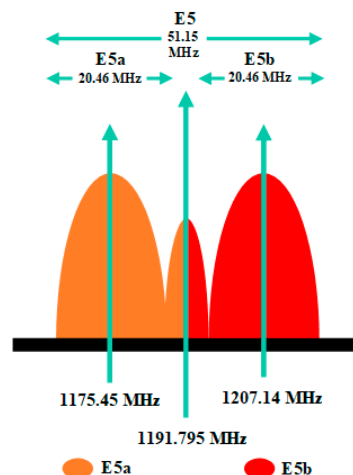


Figure 3. Galileo E5 signal power spectral density (PSD) diagram.

The E5a and E5b signals have the same signal bandwidth, and the PSD of BPSK and QPSK signal all satisfy the law of the sinc function. Therefore, the PSD of the E5a/b NJBW joint signal can be defined as

$$P_{E5a/b}(f) = \frac{1}{f_{s_a}} \left| \sin c \frac{f - f_{c_a}}{f_{s_a}} \right|^2 + \frac{1}{f_{s_b}} \left| \sin c \frac{f - f_{c_b}}{f_{s_b}} \right|^2 \quad (14)$$

where f_{s_a} and f_{s_b} represent the signal bandwidths of E5a and E5b, respectively, and their values are $f_{s_a} = f_{s_b} = 20.46$ MHz. f_{c_a} and f_{c_b} represent the carrier center frequencies of E5a and E5b, respectively, $f_{c_a} = 1175.45$ MHz, and $f_{c_b} = f_{c_a} + 30.69$ MHz = 1207.14 MHz.

Since the signal bandwidths of E5a and E5b are the same

$$f_{s_a} = f_{s_b} = f_s \quad (15)$$

Substituting Equation (15) into Equation (14), we obtain:

$$P_{E5a/b}(f) = \frac{1}{f_s} \cdot \left| \sin c \frac{f - f_{c_a}}{f_s} \right|^2 + \frac{1}{f_s} \cdot \left| \sin c \frac{f - f_{c_b}}{f_s} \right|^2 \quad (16)$$

According to the Wiener–Khinchin theorem, the ACF of the E5a/b NJBW joint signal is the Fourier transform of its PSD.

$$\Lambda_{E5a/b}(\tau) = F\{P_{E5a/b}(f)\} = F\left\{ \frac{1}{f_s} \cdot \left| \sin c \frac{f - f_{c_a}}{f_s} \right|^2 + \frac{1}{f_s} \cdot \left| \sin c \frac{f - f_{c_b}}{f_s} \right|^2 \right\} \quad (17)$$

According to the operational characteristics of Fourier transform, and $f_{c_b} = f_{c_a} + \Delta f_c$ (where $\Delta f_c = 30.69$ MHz), we can obtain

$$\Lambda_{E5a/b}(\tau) = \frac{1}{f_s} \cdot F\left\{ \left| \sin c \frac{f - f_{c_a}}{f_s} \right|^2 \right\} \left(1 + e^{j2\pi\Delta f_c\tau} \right) \quad (18)$$

According to Equation (12), it can be known that the Fourier transform of the sinc square function is a triangular function whose base length is $\frac{2}{f_s}$, and its height is f_s . Since the PSD of the TSFB E5a signal is a sinc square function, the area in the triangle is the ACF main lobe of the TSFB E5a signal, and its main lobe width is:

$$BW_{E5a} = \frac{2}{f_s} \quad (19)$$

Equation (12) was substituted into Equation (18), and then the real part of the complex number term $e^{j2\pi\Delta f_c\tau}$ in Equation (18) is taken to obtain:

$$\Lambda_{E5a/b}(\tau) = \frac{1}{f_s} \cdot \text{tri}(\tau f_s) \cdot [1 + \cos(2\pi\Delta f_c\tau)] \quad (20)$$

For the E5a and the E5b sub-bands of the Galileo E5 signal, the signal bandwidths are both $f_s = 20.46$ MHz. In addition, the center frequency interval between the two sub-bands of the E5a and the E5b is $\Delta f_c = 30.69$ MHz. The area between the closest pair of minimum value points around the ACF peak value point is the main lobe of the E5a/b NJBW joint signal, and its main lobe width is:

$$BW_{E5a/b} = \frac{1}{2\Delta f_c} - \left(-\frac{1}{2\Delta f_c} \right) = \frac{1}{\Delta f_c} \quad (21)$$

Substituting the specific values of f_s and Δf_c , the ACF main lobe width of the TSFB E5a signal is 97.8 ns, and the ACF main lobe width of the E5a/b NJBW joint signal is

32.6 ns. The ACF main lobe width of the E5a/b NJBW joint signal is 1/3 of that of the TSFB E5a signal.

2.3. Pulse-Limited Footprint of the Galileo/GNSS-R E5a/b NJBW Joint Signal

After the ACF main lobe width analysis of the Galileo/GNSS-R E5a/b NJBW joint signal is completed, the analysis of the pulse-limited footprint size of the E5a/b NJBW joint signal can be carried out. For the GNSS-R system, the size of its pulse-limited footprint can be calculated by the following equation [15]:

$$\begin{cases} a = \frac{1}{\sin \theta_R} \sqrt{\frac{R_R R_T \cdot BW}{R_R + R_T}} \\ b = \sqrt{\frac{R_R R_T \cdot BW}{R_R + R_T}} \end{cases} \quad (22)$$

where a and b represent the length of the semi-major axis and the semi-minor axis of the pulse-limited footprint ellipse, respectively, θ_R represents the elevation angle of the GNSS-R satellite, and BW represents the ACF main lobe width of the GNSS signal.

It can be known from Equation (22) that the size of the pulse-limited footprint is proportional to the quadratic root of the ACF main lobe width of the GNSS signal. It can be seen from the previous discussion that the ACF main lobe width of the E5a/b NJBW joint signal is 1/3 of the ACF main lobe width of the TSFB E5a signal. In addition, the size of the pulse-limited footprint of the E5a/b NJBW joint signal is $\sqrt{1/3} = 0.58$ times to the size of the pulse-limited footprint of the TSFB E5a signal. Correspondingly, the pulse-limited footprint resolution of the E5a/b NJBW joint signal was $\sqrt{3} = 1.73$ times higher than the pulse-limited footprint resolution of the TSFB E5a signal.

3. Results and Discussion

According to Equation (22), the main factor limiting the improvement of the pulse-limited footprint resolution is the bandwidth of the E5a/b NJBW joint signal. The bandwidth of the E5a/b NJBW joint signal is 52 MHz, and this bandwidth is twice that of the TSFB E5a signal. However, the bandwidth of the TSFB GNSS-R antennas generally does not exceed 25 MHz, which cannot meet the bandwidth requirements of the NJBW signals. Therefore, it is necessary to conduct research on the NJBW GNSS-R antennas.

In order to verify the design correctness of the GNSS-R NJBW antenna, this article designs and manufactures a Galileo/GNSS-R E5a/b NJBW antenna verification prototype and tests the voltage standing wave ratio (VSWR) and radiation pattern performance with the NJBW antenna verification prototype. In order to ensure the accuracy of the test results of the NJBW antenna verification prototype, its VSWR and radiation pattern tests are carried out in an anechoic chamber to shield the influence of the external environment on the performance of the antenna. Then, the simulation results and measured results of the E5a/b NJBW antenna verification prototype are compared.

In addition, to verify the effectiveness of the E5a/b NJBW joint signal in improving the GNSS-R pulse-limited footprint resolutions, this article introduces the measured signal bandwidth values of the E5a/b NJBW antenna verification prototype under the conditions of receiving the E5a/b NJBW joint signal and TSFB E5a signal into the simulation environment, calculates the pulse-limited footprint resolutions of the two bandwidths in this environment, and compares them.

3.1. Design of the E5a/b NJBW Antenna Verification Prototype

The structure of the E5a/b NJBW antenna verification prototype is shown in Figure 4. The antenna verification prototype consists of a radiator, a feed network, a support structure between them, and a pair of radio frequency (RF) cables. The design parameters are shown in Table 1.

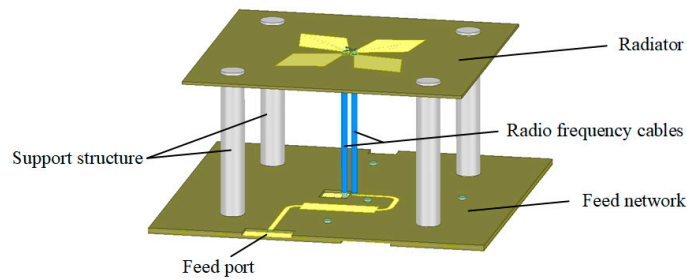


Figure 4. Schematic of the E5a/b NJBW antenna verification prototype.

Table 1. Design parameters of the E5a/b NJBW antenna verification prototype.

Design Parameter	Value
Dielectric substrate	FR4 Epoxy Glass Cloth
Dielectric constant	4.2
Loss tangent	0.02
Aperture size of the antenna (mm)	100 × 100
Thickness (mm)	50

Figure 5 shows the VSWR simulation curve of the E5a/b NJBW antenna verification prototype. It can be seen from the figure that the VSWR of the E5a/b NJBW antenna verification prototype in the E5a and E5b frequency bands is better than 1.3. At this time, the energy loss of the RF signal by the antenna is less than 2%, which can meet the requirement of simultaneously transmitting E5a and E5b signals.

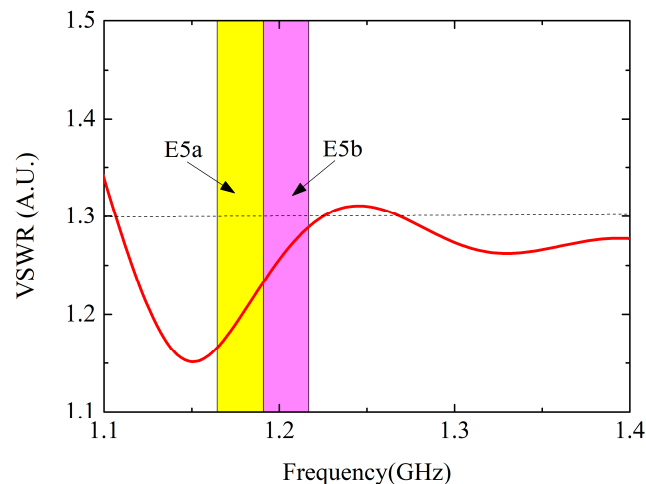


Figure 5. VSWR simulated curve of the E5a/b NJBW antenna verification prototype, where the yellow area represents the frequency range of the E5a signal, and the pink area represents the frequency range of the E5b signal, and the solid red line represents the voltage standing wave ratio of the E5a/b NJBW antenna verification prototype.

Figure 6 shows the simulated radiation pattern of the E5a/b NJBW antenna verification prototype. It can be seen from the figure that the 3 dB beam footprint width of the antenna is $\pm 45^\circ$, which is much larger than the pulse-limited footprint of the GNSS reflected signal. Therefore, the antenna can receive multiple GNSS reflection signals in a large enough range, and after coherence with the GNSS signal replica in the GNSS-R satellite, a GNSS reflection signal and its remote sensing information are obtained, thereby realizing GNSS-R sea surface wind field retrieval and height retrieval.

Table 2 shows the simulation performance statistics of the E5a/b NJBW antenna verification prototype. It can be seen from Table 2 that the antenna can realize the receiving function of Galileo E5a and E5b signals and provides an RF channel port for the GRSS-R system to receive E5a/b NJBW joint signals.

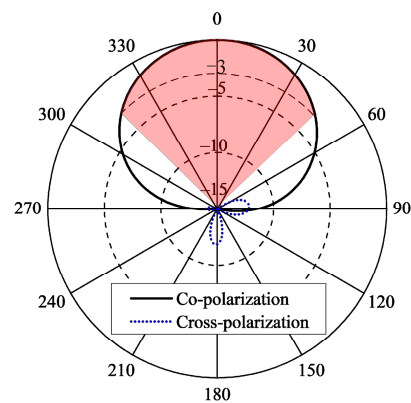


Figure 6. Simulated radiation pattern of the E5a/b NJBW antenna verification prototype, where red shading indicates the 3 dB footprint coverage of the antenna beam, where the red area represents the range of footprint of antenna beam.

Table 2. Simulation performance statistics of the E5a/b NJBW antenna verification prototype.

Antenna Parameter	Simulated Value
Antenna polarization	LHCP
Working frequency band	Galileo E5a and E5b
Working frequency	1166.22~1217.37 MHz
VSWR	<1.27
Footprint of antenna beam	The circular field of $\Phi 44.1^\circ$

3.2. Testing of the E5a/b NJBW Antenna Verification Prototype

Figure 7 shows the E5a/b NJBW antenna verification prototype, which was manufactured according to the design results above, and its VSWR and radiation pattern were tested in the anechoic chamber. The purpose of testing the VSWR is to verify the antenna's ability to receive GNSS reflected signals within the E5a/b jointed bandwidth range. In addition, the purpose of testing the radiation pattern is to verify the antenna beam footprint's width value, which is much larger than the pulse-limit footprint size. Therefore, the antenna can receive multiple GNSS reflection signals in a large enough range. Additionally, after coherence with the GNSS signal replica in the GNSS-R satellite, GNSS reflection signal information is obtained, thereby realizing GNSS-R sea surface wind field retrieval and height retrieval. Since different GNSS satellites have different PRN codes, reflected signals from different GNSS satellites can be differentiated by correlating with different replicas of the PRN code within the GNSS-R satellite.



Figure 7. The E5a/b NJBW antenna verification prototype.

The E5a/b NJBW antenna verification prototype was tested in the anechoic chamber, and the Agilent E8361A vector network analyzer was used for testing. The test is carried out in two steps. First, the vector network analyzer is directly connected to the feed port of the E5a/b NJBW antenna verification prototype, and the testing result of the antenna's VSWR is obtained. Second, the E5a/b NJBW antenna verification prototype is connected to the radiation performance testing system in the anechoic chamber, and the radiation performance testing of the E5a/b NJBW antenna verification prototype is carried out, and the testing result of the E5a/b NJBW antenna verification prototype is obtained. The testing results of the E5a/b NJBW antenna verification prototype are shown in Table 3, which are in good agreement with the design results shown in Table 2, and the difference is less than 5%, which verifies the correctness of the design.

Table 3. Measured performance statistics of the E5a/b NJBW antenna verification prototype.

Antenna Parameter	Measured Value
Antenna polarization	LHCP
Working frequency band	Galileo E5a and E5b
Working frequency	1166.22~1217.37 MHz
VSWR	<1.31
Footprint of antenna beam	The circular field of $\Phi 44.3^\circ$

The measured results of the E5a/b NJBW antenna verification prototype shown in Table 3 indicate that the performance of the E5a/b NJBW antenna verification prototype meets the requirements in the Galileo E5a and E5b frequency bands and can be applied as the receiving antenna of the GNSS-R system for the Galileo E5a and E5b NJBW joint signal.

3.3. Resolution of the E5a/b NJBW Joint Signal

3.3.1. Main Lobe Width of ACF

In the verification of the pulse-limited footprint size of the NJBW antenna verification prototype, the main factor is the signal bandwidth. Substituting the tested results of the working frequency (i.e., bandwidth) of the NJBW antenna verification prototype in Section 3.2. into the actual environmental parameters, the pulse-limited footprint resolution can be obtained when the NJBW antenna verification prototype is applied. According to Equation (13) and Equation (20), the corresponding ACF can be obtained by inverse Fourier transforming the PSD of the TSFB E5a signal and the E5a/b NJBW joint signal, respectively. In order to compare and analyze the influence of the E5a/b NJBW joint signal on the GNSS-R sea surface wind field retrieval and height retrieval, this article selects the TSFB E5a signal as a reference, and the ACF of these two signals is given in Figure 8. It can be seen from the figure that due to the periodicity of the $\cos(2\pi\Delta f_c\tau)$ term in Equation (20), the ACF of the E5a/b NJBW joint signal presents a multi-peak distribution, in which the main peak is significantly narrower than that of the TSFB E5a signal. This feature is conducive to better resolution capabilities, and it is possible to obtain a more accurate pulse-limited footprint resolution when retrieving the GNSS-R sea surface wind field.

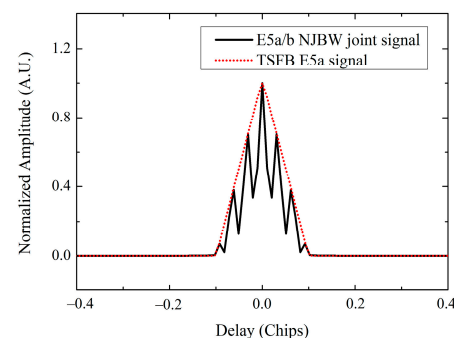


Figure 8. ACF curves of the E5a/b NJBW joint signal and the TSFB E5a signal.

3.3.2. Pulse-Limited Footprint Resolution

In order to verify the improvement effect of the E5a/b NJBW joint signal on the pulse-limited footprint resolution in the specific spaceborne GNSS-R application, this article constructed a GNSS-R in-orbit application scenario and carried out a GNSS-R pulse-limited footprint resolution assessment. The specific parameter settings of this scene are shown in Table 4.

Table 4. Environmental parameters involved in the assessment of the E5a/b NJBW joint signal applications.

Environmental Parameter	Value
GNSS satellite orbit altitude (km)	23,222
GNSS-R satellite orbit altitude (km)	400
E5a signal bandwidth (MHz)	20.46
E5a signal center frequency (MHz)	1175.45
E5b signal bandwidth (MHz)	20.46
E5b signal center frequency (MHz)	1207.14
Receiver bandwidth (MHz)	100

Figure 9 shows the comparison of the pulse-limited footprint size obtained by substituting the parameters of the TSFB E5a signal and the E5a/b NJBW joint signal into the simulation environment. It can be seen from Figure 9 that when the pulse-limited footprint located at the typical position, that is, at the nadir point of the GNSS satellite and GNSS-R satellite, is compared with the TSFB E5a signal, the nadir pulse-limit footprint size of the E5a/b NJBW joint signal reduces from 3.8 km to 2.2 km, which is 0.58 times. As the size of the pulse-limited footprint decreases, the minimum recognizable pixel size of GNSS-R becomes finer, which effectively improves the GNSS-R pulse-limited footprint resolution's performance.

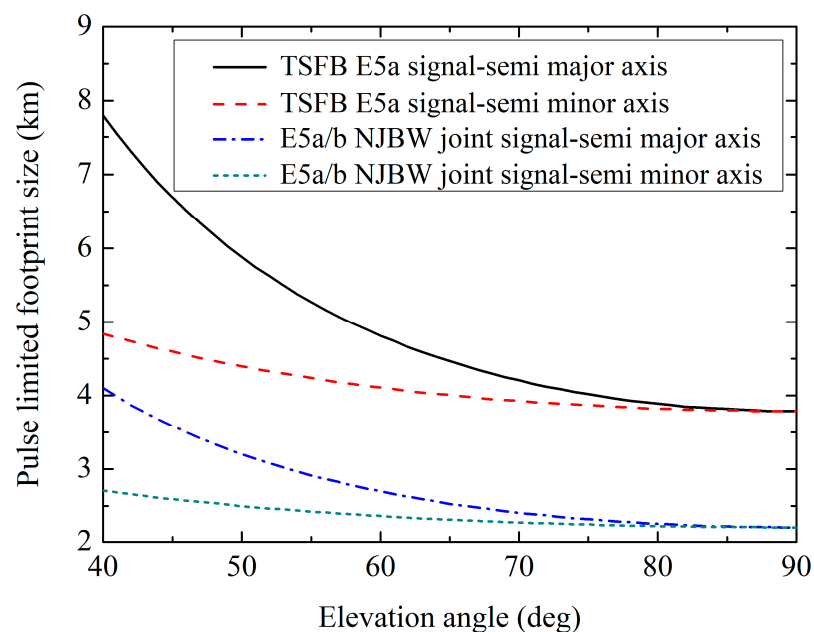


Figure 9. Pulse-limited footprint size of the E5a/b NJBW joint signal and the TSFB E5a signal.

As mentioned above, compared with the TSFB E5a signal, the pulse-limited footprint size of the GNSS-R system applying the E5a/b NJBW joint signal is narrowed by 0.58 times from 3.8 km to 2.2 km. Correspondingly, the pulse-limited footprint resolution with the E5a/b NJBW joint signal is increased to 1.72 times that of the TSFB E5a signal according to the reciprocal law with the pulse-limited footprint size ratio.

Applying the E5a/b NJBW joint signal is an effective method to improve the pulse-limited footprint resolution of GNSS-R systems. By applying the E5a/b NJBW joint signal for remote sensing, more detailed remote sensing information can be obtained than the TSFB E5a signal. This technology can support GNSS-R sea surface wind field retrieval and height retrieval remote sensing at the pulse-limited footprint resolution of the 2 km level, thereby supporting the ongoing global sea surface wind field observation based on spaceborne GNSS-R measurement methods with high pulse-limited footprint resolution.

4. Conclusions

The pulse-limited footprint size is an important indicator of the GNSS-R sea surface wind field retrieval and height retrieval system, which is directly related to the pulse-limited footprint resolution of the GNSS-R sea surface wind field observation.

- (1) In order to reduce the pulse-limited footprint size and improve the pulse-limited footprint resolution, we propose a NJBW method of jointing Galileo E5a and E5b reflected signal bandwidth based on the GNSS-R auto-correlation signal ambiguity theory. This method reduces the ACF width of the GNSS-R signal by jointing the E5a and E5b frequency bands, thereby improving the pulse-limited footprint resolution of Galileo/GNSS-R. For the Galileo E5a/b NJBW joint signal, the main lobe width of its ACF is 1/3 of that of the TSFB E5a signal, its pulse-limited footprint size is $\sqrt{1/3}$ of that of the TSFB E5a signal, and the pulse-limited footprint resolution is increased by about 1.73 times.
- (2) In order to verify the Galileo/GNSS-R NJBW method, this article designed and fabricated a Galileo/GNSS-R E5a/b NJBW antenna verification prototype. The performance of the E5a/b NJBW antenna verification prototype meets the requirements for applying in the E5a and E5b frequency bands, effectively expanding the bandwidth of the Galileo/GNSS-R RF channel and effectively expanding the Galileo/GNSS-R processed signal bandwidth. According to the tested results of the E5a/b NJBW antenna verification prototype, compared with the TSFB E5a signal, the E5a/b NJBW joint signal can reduce the pulse-limited footprint size from 3.8 km to 2.2 km, and the footprint resolution is increased by 1.72 times, which is very close to the theoretical result of the model.
- (3) According to the tested results of the Galileo/GNSS-R E5a/b NJBW antenna verification prototype, it is shown that applying the NJBW method can improve the fineness of the Galileo/GNSS-R pulse-limited footprint size and then improve the pulse-limited footprint resolution. The Galileo E5a/b NJBW method proposed in this paper provides a theoretical method basis and key technical support for the wind field retrieval and height retrieval and antenna design of the GNSS-R sea surface wind field retrieval and height retrieval verification satellite with high pulse-limited footprint resolution in the future.

Author Contributions: Writing—original draft, Z.C.; writing—review and editing, W.Z., F.W., X.L., K.X., X.M., J.S., X.T., C.Z. and X.Z. All authors have read and agreed to the published version of the manuscript.

Funding: This research was funded by the National Natural Science Foundation of China under grant 42274119, in part by the Liaoning Revitalization Talents Program under grant XLYC2002082, in part by the National Key Research and Development Plan Key Special Projects of Science and Technology Military Civil Integration (2022YFF1400500), in part by the Key Project of Science and Technology Commission of the Central Military Commission, and the Independent Research and Development Start-up Fund of Qian Xuesen Laboratory of Space Technology (Y-KC-WY-99-ZY-000-025), and in part by the National Defense Science and Technology 173 Program Technology Field Fund (2021-JCJQ-JJ-0828).

Data Availability Statement: Not applicable.

Conflicts of Interest: The authors declare no conflict of interest.

References

1. Martin-Neira, M. A passive reflectometry and interferometry system (PARIS): Application to ocean altimetry. *ESA J.* **1993**, *17*, 331–355.
2. Katzberg, S.J.; Garrison, J.L. Utilizing GPS to determine ionospheric delay over the ocean. In *NASA Technical Memo*; NASA Center for Aerospace Information: Linthicum Heights, MD, USA, 1996.
3. Garrison, J.L.; Katzberg, S.J. Detection of ocean reflected GPS signals: Theory and experiment. In Proceedings of the IEEE SOUTHEASTCON'97, Blacksburg, VA, USA, 12–14 April 1997.
4. Garrison, J.L.; Katzberg, S.J.; Hill, M.I. Effect of sea roughness on bistatically scattered range coded signals from the Global Positioning System. *Geophys. Res. Lett.* **1998**, *25*, 2257–2260. [[CrossRef](#)]
5. Shaw, P.T.; Chao, S.Y.; Fu, L.L. Sea surface height variations in the South China Sea from satellite altimetry. *Oceanol. Acta* **1999**, *22*, 1–17. [[CrossRef](#)]
6. Shum, C.; Yi, Y.; Cheng, K.; Kuo, C.; Braun, A.; Calmant, S.; Chambers, D. Calibration of JASON-1 altimeter over lake erie special issue: Jason-1 calibration/validation. *Mar. Geod.* **2003**, *26*, 335–354. [[CrossRef](#)]
7. Hausleitner, W.; Moser, F.; Desjonqueres, J.D.; Boy, F.; Picot, N.; Weingrill, J.; Mertikas, S.; Daskalakis, A. A new method of precise Jason-2 altimeter calibration using a microwave transponder. *Mar. Geod.* **2012**, *35*, 337–362. [[CrossRef](#)]
8. Maiwald, F.; Montes, O.; Padmanabhan, S.; Michaels, D.; Kitiyakara, A.; Jarnot, R.; Brown, S.T.; Dawson, D.; Wu, A.; Hatch, W.; et al. Reliable and stable radiometers for Jason-3. *IEEE J. Sel. Top. Appl. Earth Obs. Remote Sens.* **2016**, *9*, 2754–2762. [[CrossRef](#)]
9. Auber, J.C.; Bibaut, A.; Rigal, J.M. Characterization of multipath on land and sea at GPS frequencies. In Proceedings of the 7th International Technical Meeting of the Satellite Division of the Institute of Navigation (ION GPS 1994), Salt Lake City, UT, USA, 20–23 September 1994.
10. Lin, B.; Katzberg, S.J.; Garrison, J.L.; Wielick, B.A. The relationship between the GPS signals reflected from sea surface and the surface winds: Modeling results and comparisons with aircraft measurements. *J. Geophys. Res. Oceans* **1999**, *104*, 20713–20727. [[CrossRef](#)]
11. Garrison, J.L.; Katzberg, S.J. The application of reflected GPS signals to ocean remote sensing. *Remote Sens. Environ.* **2000**, *73*, 175–187. [[CrossRef](#)]
12. Katzberg, S.J.; Walker, R.A.; Roles, J.H.; Lynch, T.; Black, P.G. First GPS signals reflected from the interior of a tropical storm: Preliminary results from Hurricane Michael. *Geophys. Res. Lett.* **2001**, *28*, 1981–1984. [[CrossRef](#)]
13. Elfouhaily, T.; Chapron, B.; Katsaros, K.; Vandemark, D. A unified directional spectrum for long and short wind-driven waves. *J. Geophys. Res. Ocean.* **1997**, *102*, 15781–15796. [[CrossRef](#)]
14. Zavorotny, V.U.; Voronovich, A.G. Scattering of GPS signals from the ocean with wind remote sensing application. *IEEE Trans. Geosci. Remote Sens.* **2000**, *38*, 951–964. [[CrossRef](#)]
15. Hajj, G.A.; Zuffada, C. Theoretical description of a bistatic system for ocean altimetry using the GPS signal. *Radio Sci.* **2003**, *38*, 1–19. [[CrossRef](#)]
16. Valencia, E.; Camps, A.; Marchan-Hernandez, J.F.; Hyuk, P.; Bosch-Lluis, X.; Rodriguez-Alvarez, N.; Ramos-Perez, I. Ocean surface's scattering coefficient retrieval by delay-Doppler map inversion. *IEEE Geosci. Remote Sens. Lett.* **2011**, *8*, 750–754. [[CrossRef](#)]
17. Gleason, S.; Hodgart, S.; Sun, Y.; Gommenginger, C.; Mackin, S.; Adjrard, M.; Unwin, M. Detection and processing of bistatically reflected GPS signals from low earth orbit for the purpose of ocean remote sensing. *IEEE Trans. Geosci. Remote Sens.* **2005**, *43*, 1229–1241. [[CrossRef](#)]
18. Li, C.; Huang, W. An algorithm for sea-surface wind field retrieval from GNSS-R delay-Doppler map. *IEEE Geosci. Remote Sens. Lett.* **2014**, *11*, 2110–2114.
19. Clarizia, M.P.; Ruf, C.S.; Jales, P.; Gommenginger, C. Spaceborne GNSS-R minimum variance wind speed estimator. *IEEE Trans. Geosci. Remote Sens.* **2014**, *52*, 6829–6843. [[CrossRef](#)]
20. Zheng, W.; Xu, H.; Zhong, M.; Yun, M. Improvement in the recovery accuracy of the lunar gravity field based on the future Moon-ILRS spacecraft gravity mission. *Surv. Geophys.* **2015**, *36*, 587–619. [[CrossRef](#)]
21. Wu, F.; Zheng, W.; Li, Z.; Liu, Z. Improving the GNSS-R specular reflection point positioning accuracy using the gravity field normal projection reflection reference surface combination correction method. *Remote Sens.* **2019**, *11*, 33. [[CrossRef](#)]
22. Wu, F.; Zheng, W.; Li, Z.; Liu, Z. Improving the positioning accuracy of satellite-borne GNSS-R specular reflection point on sea surface based on the ocean tidal time-varying elevation correction positioning method. *Remote Sens.* **2019**, *11*, 1626. [[CrossRef](#)]
23. Liu, Z.; Zheng, W.; Wu, F.; Li, X.; Zhu, C.; Liu, Z.; Ma, X. Improving the number of sea surface altimetry reflected signals received by GNSS-R satellite based on the new satellite-borne nadia antenna receiving signal-to-noise ratio model. *Remote Sens.* **2019**, *11*, 1–16.
24. Wu, F.; Zheng, W.; Liu, Z.; Sun, X. Improving the specular point positioning accuracy of ship-borne GNSS-R observations in China's Seas based on a new instantaneous sea reflection surface model. *Front. Earth Sci.* **2021**, *9*, 662–1–662–11. [[CrossRef](#)]
25. Cui, Z.; Zheng, W.; Wu, F.; Kang, G.; Li, Z.; Wang, Q.; Cui, Z. Improving GNSS-R sea surface altimetry precision based on the novel dual circularly polarized phased array antenna model. *Remote Sens.* **2021**, *13*, 2974. [[CrossRef](#)]
26. Wang, Q.; Zheng, W.; Wu, F.; Xu, A.; Zhu, H.; Liu, Z. A new GNSS-R altimetry algorithm based on machine learning fusion model and feature optimization to improve the precision of sea surface height retrieval. *Front. Earth Sci.* **2021**, *9*, 758. [[CrossRef](#)]

27. Sun, X.; Zheng, W.; Wu, F.; Liu, Z. Improving the iGNSS-R ocean altimetric precision based on the coherent integration time optimization Model. *Remote Sens.* **2021**, *13*, 4715. [[CrossRef](#)]
28. Liu, Z.; Zheng, W.; Wu, F.; Kang, G.; Sun, X.; Wang, Q. Relationship between altimetric quality and along-track spatial resolution for iGNSS-R sea surface altimetry: Example for the airborne experiment. *Front. Earth Sci.* **2021**, *9*, 1119. [[CrossRef](#)]
29. Yan, Z.; Zheng, W.; Wu, F.; Wang, C.; Zhu, H.; Xu, A. Correction of atmospheric delay error of airborne and spaceborne GNSS-R sea surface altimetry. *Front. Earth Sci.* **2022**, *10*, 730551. [[CrossRef](#)]
30. Wang, Q.; Zheng, W.; Wu, F.; Zhu, H.; Xu, A.; Shen, Y.; Zhao, Y. Improving the SSH retrieval precision of spaceborne GNSS-R based on a new grid search multihidden layer neural network feature optimization method. *Remote Sens.* **2022**, *14*, 3161. [[CrossRef](#)]
31. Zavorotny, V.U.; Gleason, S.; Cardellach, E.; Camps, A. Tutorial on remote sensing using GNSS bistatic radar of opportunity. *IEEE Geosci. Remote Sens. Mag.* **2014**, *2*, 8–45. [[CrossRef](#)]
32. Unwin, M.; Gleason, S.; Brennan, M. The space GPS reflectometry experiment on the UK disaster monitoring constellation satellite. In Proceedings of the 16th International Technical Meeting of the Satellite Division of The Institute of Navigation (ION GPS/GNSS 2003), Portland, OR, USA, 9–12 September 2003.
33. Jales, P.; Unwin, M. *MERRByS Product Manual: GNSS Reflectometry on TDS-1 with the SGR-ReSI*; Surrey Satellite Technology Ltd.: Guildford, UK, 2017.
34. Carreno-Luengo, H.; Camps, A.; Via, P.; Munoz, J.F.; Cortiella, A.; Vidal, D.; Jane, J.; Catarino, N.; Hagenfeldt, M.; Palomo, P.; et al. 3Cat-2—An experimental nanosatellite for GNSS-R earth observation: Mission concept and analysis. *IEEE J. Sel. Top. Appl. Earth Obs. Remote Sens.* **2016**, *9*, 4540–4551. [[CrossRef](#)]
35. Ruf, C.; Chang, P.; Clarizia, M.P.; Posselt, D.; Majumdar, S.; Gleason, S.; Morris, M. *CYGNSS Handbook*; Michigan Publishing: Ann Arbor, MI, USA, 2016.
36. Available online: <https://china.huanqiu.com/article/9CaKrnKkO1r> (accessed on 12 July 2019).
37. Martin, F.; Camps, A.; Park, H.; D’Addio, S.; Martin-Neira, M.; Pascual, D. Cross-correlation waveform analysis for conventional and interferometric GNSS-R approaches. *IEEE J. Sel. Top. Appl. Earth Obs. Remote Sens.* **2014**, *7*, 1560–1572. [[CrossRef](#)]
38. Martin-Neira, M.; D’Addio, S.; Buck, C.; Floury, N.; Prieto-Cerdeira, R. The PARIS ocean altimeter in-orbit demonstrator. *IEEE Trans. Geosci. Remote Sens.* **2011**, *49*, 2209–2237. [[CrossRef](#)]
39. Li, W.; Rius, A.; Fabra, F.; Martin-Neira, M.; Cardellach, E.; Ribo, S.; Yang, D. The impact of inter-modulation components on interferometric GNSS-reflectometry. *Remote Sens.* **2016**, *8*, 1013. [[CrossRef](#)]
40. Beckmann, P.; Spizzichino, A. *The Scattering of Electromagnetic Waves from Rough Surfaces*; Artech House Inc.: Norwood, MA, USA, 1987.
41. Rytov, S.M.; Kravtsov, Y.A.; Tatarskii, V.I. *Principles of Statistical Radiophysics 2. Correlation Theory of Random Processes*; Springer: Berlin, Germany, 1988.
42. Clifford, S.F.; Tatarskii, V.I.; Voronovich, A.G.; Zavorotny, V.U. GPS sounding of ocean surface waves: Theoretical assessment. In Proceedings of the 1998 IEEE International Geoscience and Remote Sensing, Seattle, WA, USA, 6–10 July 1998.
43. Bass, F.G.; Fuks, I.M. *Wave Scattering from Statistically Rough Surfaces: International Series in Natural Philosophy*; Elsevier Science: Amsterdam, The Netherlands, 2013.
44. Voronovich, A.G. *Wave Scattering from Rough Surfaces*; Springer Science & Business Media: Berlin, Germany, 2013.
45. Komjathy, A.; Zavorotny, V.U.; Axelrad, P.; Born, G.H.; Garrison, J.L. GPS signal scattering from sea surface: Wind speed retrieval using experimental data and theoretical model. *Remote Sens. Environ.* **2000**, *73*, 162–174. [[CrossRef](#)]
46. Pei, Y.; Notarpietro, R.; Savi, P.; Cucca, M.; Dovic, F. A fully software GNSS-R receiver for soil monitoring. *Int. J. Remote Sens.* **2014**, *35*, 2378–2391. [[CrossRef](#)]
47. Tonder, V.; Schwardt, L.; Faustmann, A.; Gilmore, J. Bispectra of simulated GPS data for potential RFI mitigation. In Proceedings of the 2022 3rd URSI Atlantic and Asia Pacific Radio Science Meeting (AT-AP-RASC), Gran Canaria, Spain, 30 May–4 June 2022.
48. Tang, X.; Yuan, M.; Wang, F. Analysis of GPS P (Y) signal power enhancement based on the observations with a semi-codeless receiver. *Satell. Navig.* **2022**, *3*, 26. [[CrossRef](#)]
49. Borre, K.; Fernández-Hernández, L.; López-Salcedo, J.A.; Bhuiyan, M.Z.H. *GNSS Software Receivers*; Cambridge University Press: Cambridge, UK, 2022.
50. Bastide, F.; Chatre, E.; Macabiau, C.; Routurier, B. GPS L5 and Galileo E5a/E5b signal-to-noise density ratio degradation due to DME/TACAN signals: Simulations and theoretical derivation. In Proceedings of the 2004 National Technical Meeting of The Institute of Navigation, San Diego, CA, USA, 26–28 January 2004.
51. Ali, I.; Khan, S.; Ali, M.; Mujeeb, K. Efficient and unique learning of the complex receiver structure of Galileo E5 AltBOC using an educational software in Matlab. In Proceedings of the 2023 4th International Conference on Computing, Mathematics and Engineering Technologies (iCoMET), Sukkur, Pakistan, 17–18 March 2023.

Disclaimer/Publisher’s Note: The statements, opinions and data contained in all publications are solely those of the individual author(s) and contributor(s) and not of MDPI and/or the editor(s). MDPI and/or the editor(s) disclaim responsibility for any injury to people or property resulting from any ideas, methods, instructions or products referred to in the content.